NASA TECHNICAL NOTE

NASA TN D-3221

NASA TN D-3221

TURBULENCE, HEAT-TRANSFER, AND BOUNDARY LAYER MEASUREMENTS IN A CONICAL NOZZLE WITH A CONTROLLED INLET VELOCITY PROFILE

by Donald R. Boldman, James F. Schmidt, and Anthony Fortini

Lewis Research Center
Cleveland, Ohio

NATIONAL AERONAUTICS AND SPACE ADMINISTRATION • WASHINGTON, D. C. MARCH 1966

NASA TN D-3221

TURBULENCE, HEAT-TRANSFER, AND BOUNDARY LAYER MEASUREMENTS IN A CONICAL NOZZLE WITH A CONTROLLED INLET VELOCITY PROFILE

By Donald R. Boldman, James F. Schmidt, and Anthony Fortini

Lewis Research Center
Cleveland, Ohio

NATIONAL AERONAUTICS AND SPACE ADMINISTRATION

For sale by the Clearinghouse for Federal Scientific and Technical Information
Springfield, Virginia 22151 – Price $0.40

TURBULENCE, HEAT-TRANSFER, AND BOUNDARY LAYER MEASUREMENTS IN A CONICAL NOZZLE WITH A CONTROLLED INLET VELOCITY PROFILE

by Donald R. Boldman, James F. Schmidt, and Anthony Fortini

Lewis Research Center

SUMMARY

Turbulence, heat-transfer, and boundary layer measurements were obtained in a conical nozzle operating in air at a nominal total temperature and pressure of 960° R and 300 psia, respectively. Experimental heat-transfer coefficients were compared to values determined by three prediction techniques; namely, (1) Nusselt number correlation, (2) a compressible boundary layer theory, and (3) an incompressible boundary layer theory. Methods (1) and (2) yielded nozzle heat-transfer coefficients that were appreciably higher than experimental values; however, method (3) predicted the nozzle heat-transfer coefficients very well yielding results that were within about 2 percent of the experimental values at the throat.

In part of the investigation a simulated nuclear reactor core turbulence generator installed 3 inches upstream of the cylindrical inlet failed to alter the nozzle heat-transfer coefficients. In addition, the turbulence generator had essentially no effect on the boundary layer temperature profiles in the nozzle.

INTRODUCTION

An accurate accounting of cooling requirements for nozzles subjected to the high-energy gaseous environments usually associated with chemical and nuclear rockets necessitates the prediction of local gas-side heat-transfer coefficients. Accuracy in the prediction of the convective heat-transfer coefficients is especially important for nuclear rocket nozzles since the regenerative cooling capabilities may be marginal.

A conventional method of predicting the local heat-transfer coefficients in rocket nozzles consists of employing empirical Nusselt number correlations (ref. 1), based on some reference condition. These Nusselt number correlations completely neglect the effects of pressure gradient, variation in wall temperature, and boundary layer growth. Experience has shown that Nusselt-type correlations do not provide the accuracy required in the prediction of nuclear rocket nozzle heat-transfer rates. Therefore, it is desirable to use a more

fundamental approach to the determination of gas-side heat-transfer coefficients, which involves a knowledge of the boundary layer characteristics. For example, the widely used compressible boundary layer theory discussed in references 2 and 3 provides a means of predicting boundary layer development and heat transfer for flows through convergent-divergent nozzles.

The boundary layer theory of reference 3 consists of a simultaneous solution of the integral momentum and energy equations. Although a pressure gradient term is included in the momentum equation, a modified flat-plate theory was used for the skin friction coefficient and Reynolds analogy. In addition, 1/7-power velocity and temperature profiles were used. An incompressible boundary layer theory (ref. 4) based completely on flat-plate theory is also applied to this conical nozzle flow study.

In using these boundary layer theories for predicting heat transfer, an estimate of the initial boundary layer conditions in the nozzle is necessary. The problem of determining these initial conditions is compounded by factors such as turbulence level and boundary layer transition phenomena. Therefore, in experimental studies of heat transfer, these factors allude to boundary layer and turbulence measurements as well as controlled inlet flows.

In reference 5, the results of a nozzle heat-transfer investigation conducted in a hot-air facility show rather large differences between measured heat-transfer rates and values predicted by (1) a Nusselt correlation and (2) an application of the boundary layer method of reference 2 as modified in reference 6. The discrepancy was characterized by experimental heat-transfer coefficients that were lower in the throat section and higher in the convergent section of the nozzle than predicted values. These air-facility data tend to parallel the heat-transfer results obtained from actual firings of a full-scale hydrogen-oxygen rocket (ref. 7).

The present investigation was conducted to explore further the nozzle heat-transfer problem with particular emphasis on the convergent part of the nozzle. This part of the nozzle is of interest because it is a region of flow acceleration that influences the boundary layer characteristics and, subsequently, the heat transfer in the throat region of the nozzle. The primary objectives of the study were (1) to obtain heat-transfer and boundary layer measurements within the cylindrical inlet and convergent portions of the nozzle and to apply the results in the evaluation of various heat-transfer prediction methods and (2) to observe the effects of upstream turbulence on nozzle heat-transfer rates and boundary layer profiles.

The experimental equipment comprises a cylindrical inlet followed by a conical nozzle that was instrumented with static pressure taps and plug-type heat-flux meters. A boundary layer suction mechanism was used to remove the upstream boundary layer and to produce a zero boundary layer thickness at the cylindrical approach section. Boundary layer temperatures and pressure surveys were conducted approximately midway in the cylindrical inlet and at one station in the convergent part of the nozzle. A hot wire located in a plane 1/4 inch upstream of the cylindrical inlet was used to determine the turbulence level for an incoming air flow, which was maintained at a nominal stagnation pressure

of 300 pounds per square inch absolute and a temperature of 960° R.

SYMBOLS

A	probe station (tables I and IV)
a	heat-meter thermocouple nearest gas side of nozzle wall
B	probe station (table I)
b	heat-meter thermocouple
C	probe station (tables I and IV)
C_f	skin friction coefficient
C_p	specific heat of gas at constant pressure
$\mathscr{C}$	constant of integration
c	heat-meter thermocouple nearest coolant side of nozzle wall
D	diameter
h	heat-transfer coefficient
i	enthalpy
K	thermal conductivity of Inconel
k	thermal conductivity of air
k_o	intercept of conductivity of data at 0° F
L	length
m	slope of conductivity data
Nu	Nusselt number
P	pressure
Pr	Prandtl number
q	heat flux
R	inlet or nozzle radius at probe station
Re_D	Reynolds number based on nozzle diameter

Re_θ Reynolds number based on momentum thickness

r_c nozzle-throat radius of curvature

T temperature

t heat-flux meter shaft temperature

u velocity

u^+ dimensionless velocity

x axial coordinate measured from nozzle throat

y distance from wall

y^+ dimensionless distance from wall

β angular position of nozzle instrumentation (table I)

ϵ area ratio

λ temperature difference ratio

μ viscosity

φ energy thickness

ρ density

θ momentum thickness

τ shear stress

Subscripts:

ad adiabatic

av average

e free-stream edge of boundary layer

i based on enthalpy

0 total condition in plenum

ref reference enthalpy condition

s static condition

T local stagnation condition

t throat

w wall condition

Superscripts:

- time-averaged value

' pertaining to fluctuations from time average

APPARATUS

The nozzle heat-transfer facility is composed of (1) a heat exchanger, (2) a plenum and bypass flow mechanism, (3) a water-cooled test nozzle, and (4) an exhaust system. A schematic diagram of the facility is shown in figure 1.

Heat Exchanger

A jet-engine combustor was used to heat the coils of the heat exchanger through which passed high-pressure dry air. The air was heated to a stagnation temperature of 960° R at a pressure of 300 pounds per square inch absolute.

Plenum and Bypass Bleed Mechanism

The air passed from the heat exchanger through a diffuser into a 14-inch

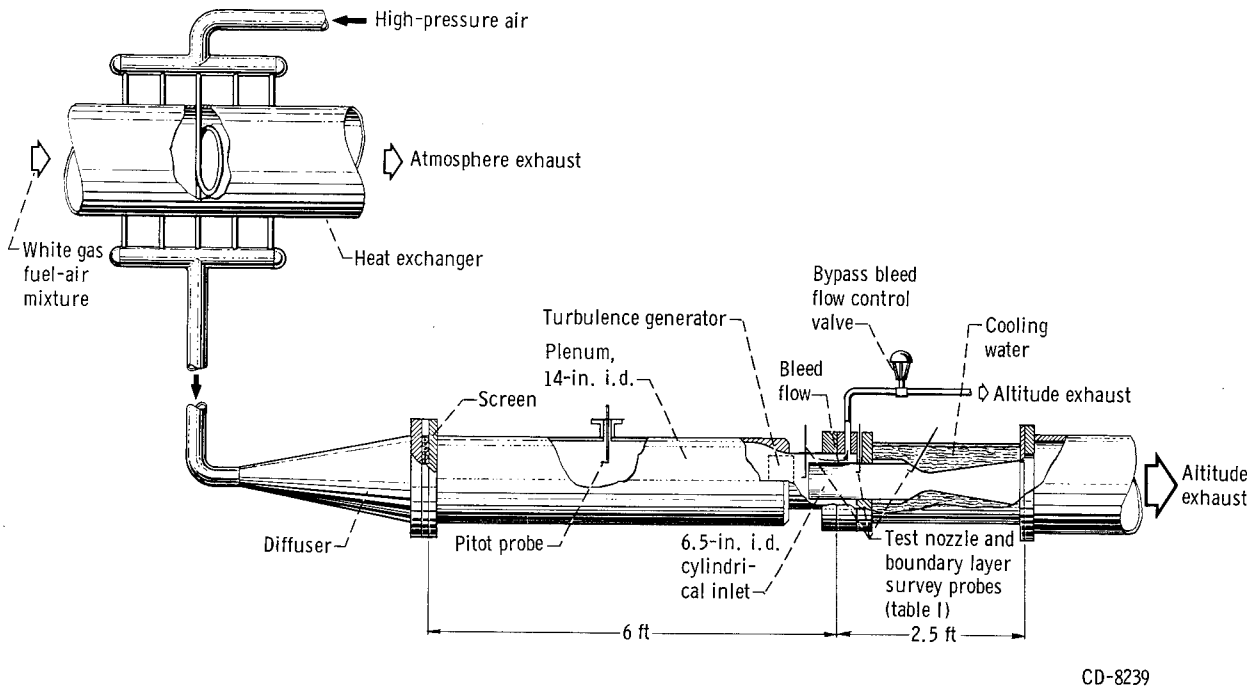

Figure 1. - Schematic diagram of nozzle heat-transfer facility.

diameter plenum. A 30-mesh screen was installed between the diffuser and plenum to provide uniform flow. The plenum was a 14-inch-inside-diameter by 6-foot-long chamber that converged to a diameter of 8.4 inches at the cylindrical inlet of the nozzle. Pitot pressure surveys in the plenum indicated that the profile is radially uniform to within 0.5 inches of the wall. The velocity in the plenum was about 17 feet per second with the bleed flow adjusted to give a uniform velocity profile across the cylindrical approach section. This velocity was sufficiently low to yield static-to-total temperature and pressure ratios of virtually 1.0.

A flow bypass manifold was used to remove the boundary layer along the plenum wall. The bleed-flow annulus height was 0.9 inch at the cylindrical inlet, a spacing which was confirmed experimentally to be adequate for removal of the plenum boundary layer. Bleed flow rates were adjusted by means of a pneumatically controlled valve which operated in a critical flow mode.

Cylindrical Inlet and Nozzle Configuration

An uncooled (adiabatic) approach section with a 17-inch length by 6.5-inch inside diameter was used in the investigation. The cylindrical inlet was machined from AISI 304 stainless-steel pipe to a wall thickness of 0.25 inch. The exterior surface of the inlet was contoured to provide a leading-edge radius of 0.03 inch.

In part of the investigation, a turbulence generator (fig. 2) was installed 3 inches upstream of the cylindrical inlet to measure the effects of upstream turbulence on the nozzle heat-transfer coefficients. The geometry of the turbulence generator was identical to the simulated nuclear reactor core turbulence generator described in reference 5; however, in that investigation the generator was located 0.85 inch upstream of the contraction section of the nozzle.

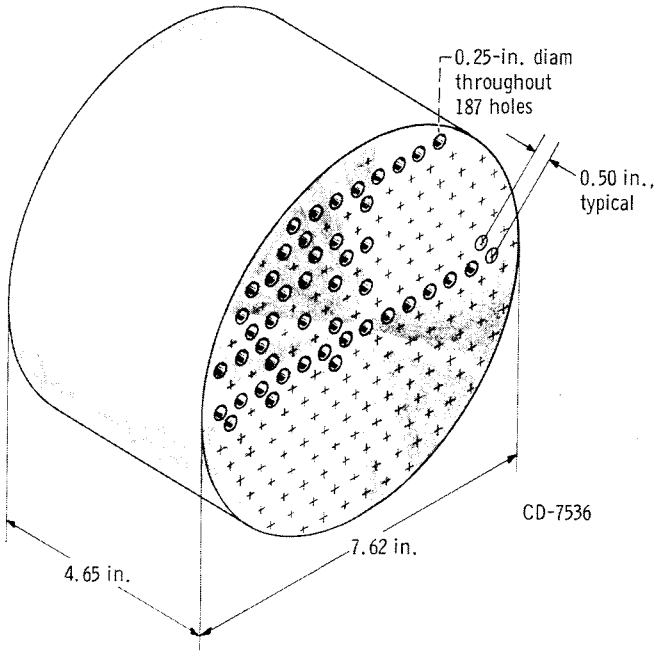

Figure 2. - Upstream turbulence generator (reactor core simulator).

The cylindrical approach section was attached to a 30°-half-angle convergent, 15°-half-angle divergent water-cooled conical nozzle. Flow disturbances resulting from the sharp corner formed by the intersection of the inlet and nozzle were assumed to be negligible. The radius of curvature of the nozzle was equal to the throat diameter (1.492 in.). The exit diameter of the nozzle was 7.4 inches corresponding to a Mach number of approximately 5. The nozzle configuration and a list of coordinates are shown in table I.

TABLE I. - NOZZLE INSTRUMENTATION AND BOUNDARY LAYER PROBE STATIONS

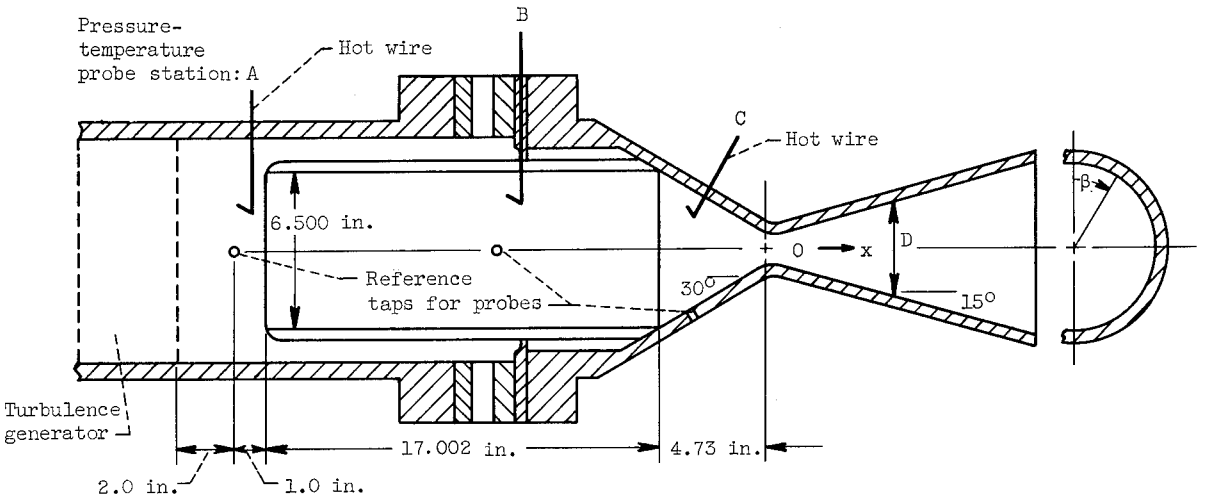

[Cylindrical inlet length-to-diameter ratio, L/D, 2.62; ratio of nozzle-throat curvature radius to throat diameter, r_c/D_t, 1.0.]

Pressure tap	Heat-flux meter	Angular position, β, deg		Axial distance, x, in.	Diameter, D, in.
		Pressure tap	Heat-flux meter		
1	1	231.4	51.4	-4.515	6.230
2	2	128.6	308.6	-3.515	5.080
3	3	180.0	0	-2.512	3.922
4	4	231.4	51.4	-2.158	3.512
5	5	282.9	102.9	-1.812	3.112
6	6	334.3	154.3	-1.460	2.710
7	7	25.7	205.7	-1.110	2.304
8	8	77.2	257.2	-.613	1.754
8a	-	102.9	-----	-.360	1.576
9	9	128.6	308.6	-.175	1.512
10	10	180.0	0	0	1.492
11	11	231.4	51.4	.130	1.502
12	12	282.9	102.9	.255	1.532
13	13	334.3	154.3	.392	1.600
14	14	25.7	205.7	.634	1.724
15	15	77.2	257.2	1.221	2.042
16	16	180.0	0	2.736	2.846
17	17	180.0	0	5.468	4.316
18	18	180.0	0	8.201	5.780
19	19	180.0	0	11.032	7.308

Pressure probe	Tempera-ture probe	Angular position, β, deg		Axial distance, x, in.	Diameter, D, in.
		Pressure probe	Tempera-ture probe		
A	A	335.0	25.0	-22.732	-----
B	B	60.0	120.0	-12.327	6.500
C	C	335.0	25.0	-2.512	3.922

The nozzle was machined from a forged billet of AISI 304 stainless steel. A wall thickness of 0.5 inch was selected because of its compatibility with the size of the heat-flux meters. Nozzle cooling water was directed axially over the nozzle by means of a lucite shroud. The coolant flow velocity was maintained such that it produced a net temperature rise of only 2° F.

Exhaust System

The nozzle was connected to a 24-inch-diameter exhaust duct by a thin flexible wafer flange, which yielded to nozzle growth and minimized radial heat conduction. The exhaust pressure, nominally 2 pounds per square inch absolute, was generally sufficient to avoid nozzle flow separation (noted occasionally at the downstream measuring station).

INSTRUMENTATION

The basic instrumentation was concerned with the measurement of temperatures, pressures, and turbulence levels. Temperatures along the heat-flux meters were used in the determination of local heat-transfer rates and wall temperatures for the nozzle. Instrumentation stations for the nozzle as well as the probing stations are listed in table I. In addition to the stations listed in table I, five static pressure and wall temperature stations were located along the cylindrical inlet. Wall temperatures were measured on the inner and outer surfaces of the inlet at each station. Static pressures were measured on the inner surface except for the upstream station at which static pressure measurements were obtained on both sides of the leading edge. The leading-edge pressure difference was used to establish the bypass flow rate.

Pressure

The plenum pressure and nozzle static pressures 8a, 9, and 10, were measured with Bourdon tube gages having an accuracy of 0.25 percent of full scale. The cylindrical inlet and remainder of the nozzle static pressures were measured by means of manometers connected differentially. Manometer fluids consisting of mercury, acetylene tetrabromide, and dibutyl phthalate were selectively used to obtain the maximum sensitivity at each station. Manometer fluid temperature corrections were applied to the data.

Boundary layer total pressure measurements in the cylindrical inlet and nozzle were obtained with a miniaturized pitot probe sketched in figure 3. Prior to shaping the pressure sensing tube, it was necessary to vacuum anneal the 0.028-inch-outside-diameter by 0.006-inch-wall AISI 304 stainless-steel hypodermic tubing. The tubing was annealed to a hardness that permitted the shaping and honing of a sharp inlet (lip thickness of approx zero in.) without cracking or tearing. The probe tip had a rectangular geometry with inside dimensions of 0.002 inch by 0.030 inch wide.

The probe traverse was terminated 0.002 inch from the wall by means of a

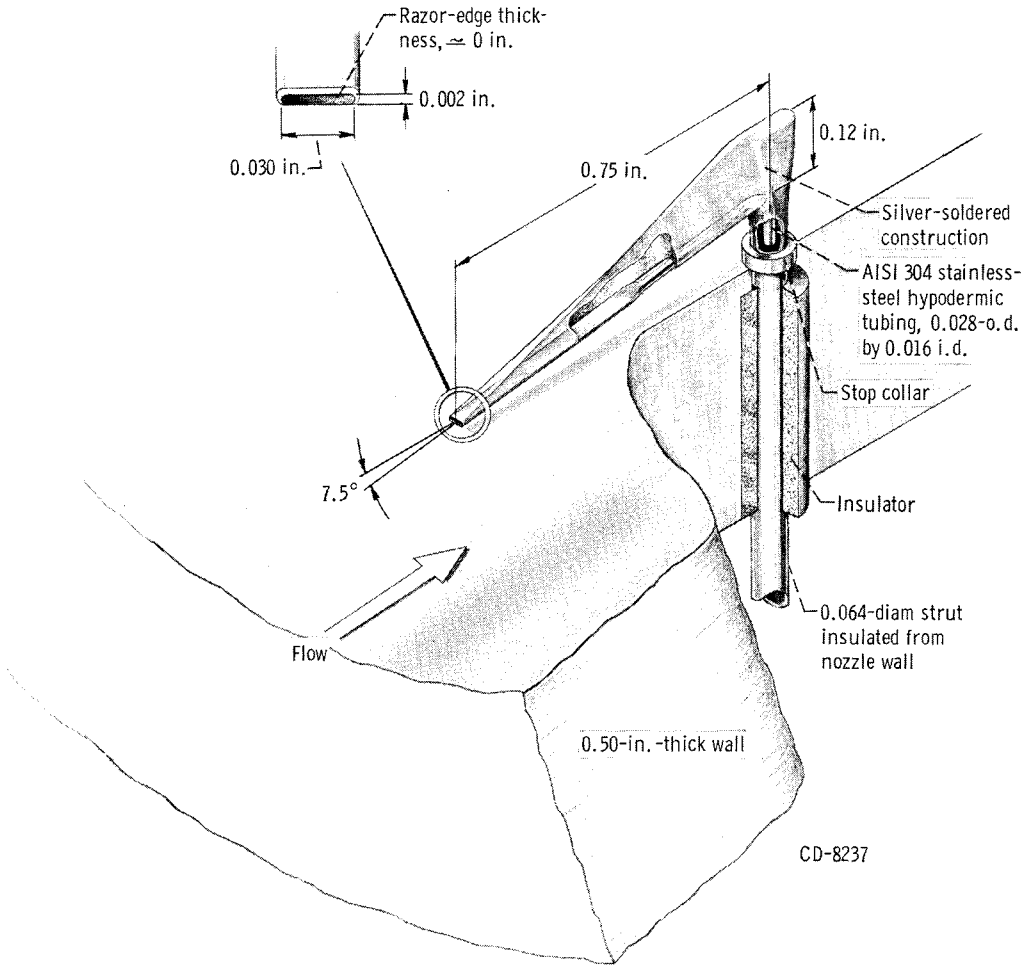

Figure 3. - Boundary layer pressure probe.

collar located on the strut of the probe. When electrical contact was made between the collar and the nozzle wall, the resulting short circuit opened the contacts of a relay which, in turn, stopped the actuator motor. The collar stop was required to avoid contact between the nozzle wall and annealed tip. Attempts to stop the probe without a collar resulted in damage to the razor-edge tip.

The pitot probes were calibrated for velocity-head recovery factor over a simulated boundary layer Mach number range. Variation of the Mach number up to a value of 0.1 had virtually no effect on the recovery factor. Recovery factors, which varied from about 97 to 99 percent, introduced negligible error in the velocity profile.

The boundary layer pressure probes were connected to dibutyl phthalate U-tube manometers that were referenced to the static pressure at the same station.

In certain tests a modified pitot probe having a tempered stainless-steel tip was close coupled to a pressure transducer to obtain measurements in the region near the wall. The output of the pressure transducer was monitored on an X-Y recorder.

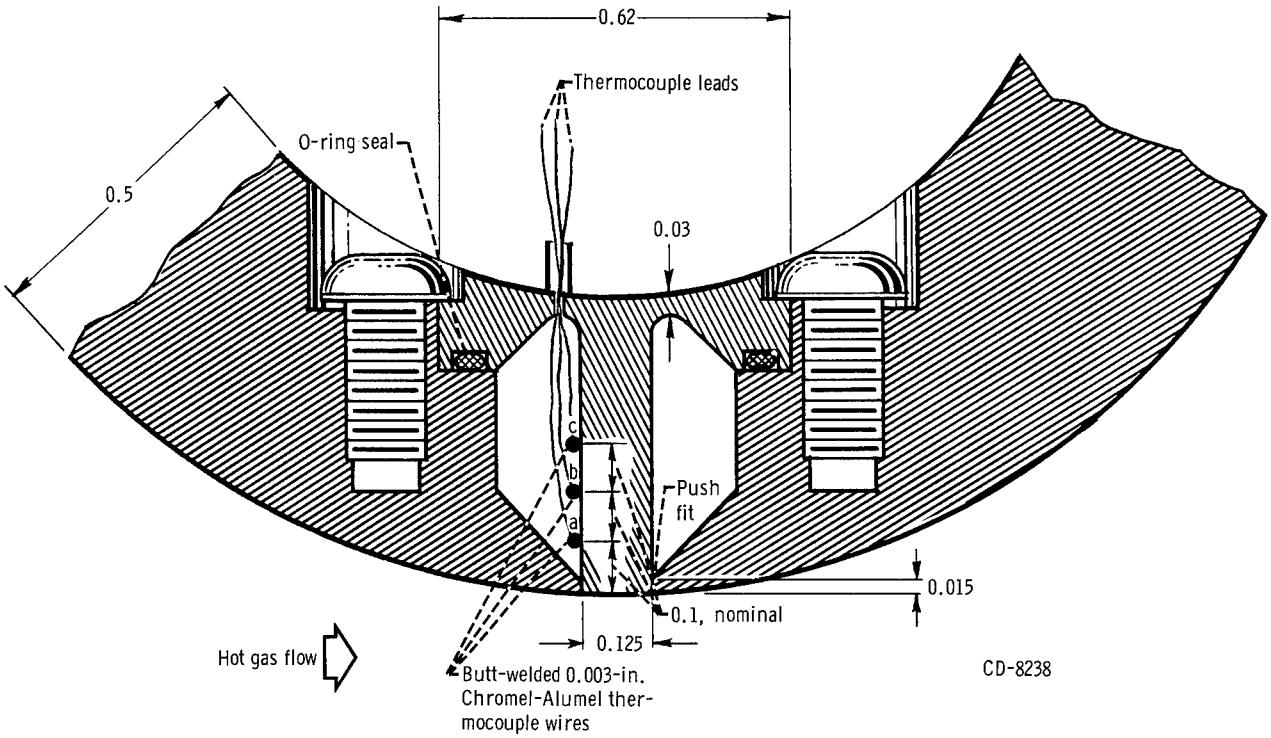

Figure 4. - Inconel heat-flux meter at nozzle throat. (All dimensions in inches.)

Temperature and Local Heat Flux

Steady-state measurements of gas-side wall temperature and local heat-transfer rates were obtained by an Inconel plug-type heat-flux meter of the type described in reference 5. A sketch of the heat-flux meter is shown in figure 4. The 0.125-inch-diameter shaft contained three Chromel-Alumel 0.003-inch wire thermocouples, spot welded in an inert gas environment to the shaft. A calibration of thermal conductivity as a function of temperature for the Inconel is given in reference 5.

$$(K = 1.307 \times 10^{-7}\ t\ (^{\circ}F) + 1.704 \times 10^{-4}\ \ Btu/(sec)(in)(^{\circ}F))$$

This equation represents the calibration data within ±4 percent for a temperature range of 200° to 1000° F. Nineteen of these heat-flux meters were installed in the nozzle, each located 180° from the static pressure tap in the same plane. Heat-flux meter locations are given in table I. The cylindrical inlet section inside and outside wall temperatures and the total temperature of the gas were measured with Chromel-Alumel thermocouples. All the aforementioned temperatures were recorded on an automatic voltage digitizer and paper tape system.

Plug-type heat-flux meters can be subject to large errors resulting from conduction through the flange between the nozzle wall and the plug. The plugs

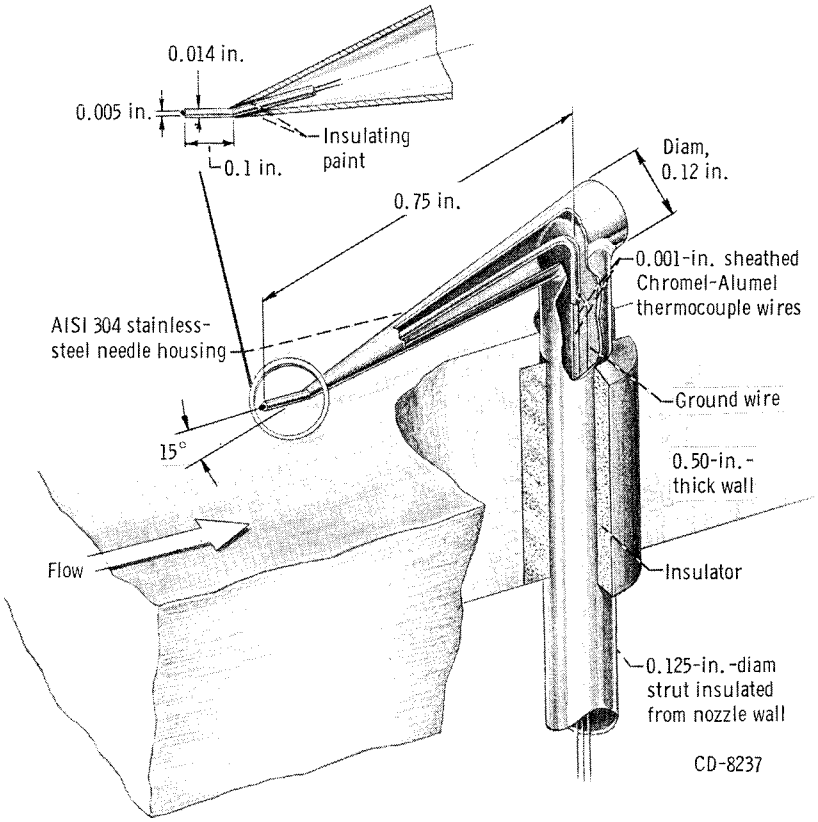

Figure 5. - Boundary layer temperature probe.

used in this investigation were installed with a light push fit in order to provide a contacting interface between the plug and the thin (0.015 in.) flange at the gas-side wall of the nozzle. The effectiveness of the contacting interface in reducing the heat exchange between the plug and the wall depends primarily on the metallic contacting pressure and gas pressure in the interface region. Estimates of the error in measured heat-transfer coefficients resulting from the conduction heat transfer indicate that the experimental heat-transfer coefficients should be multiplied by 0.9 with an uncertainty of ±10 percent.

Total temperature profiles in the boundary layer were obtained with a miniaturized probe of the type shown in figure 5. A commercial Chromel-Alumel thermocouple having a wire diameter of 0.001 inch was housed in a conical afterbody, which was silver brazed to a 0.125-inch-outside-diameter support strut. The metallic sheath surrounding the thermocouple was electrically insulated from the body of the probe so that traversing motion could be stopped on contact with the nozzle wall by the same technique used for the pressure probes. The thermocouple ball junction had a diameter of 0.005 inch; however, the sheath diameter of 0.014 inch limited the thermocouple to a minimum distance of 0.007 inch from the wall.

The probe temperature recovery factor was assumed to be 100 percent since Mach numbers were low (Mach number, $\leq$ 0.08). Also, probe heat losses were assumed to be negligible.

The boundary layer temperature probes were referenced to the stagnation

temperature, and the resulting differential temperature signal was monitored on an X-Y recorder.

Turbulence

Turbulence intensity profiles were obtained 0.25 inch upstream of the cylindrical inlet by means of a commercial hot-film sensor and a constant temperature compensating anemometer. In tests incorporating the turbulence generator, centerline values of turbulence intensity were also measured in the convergent part of the nozzle (Mach number, 0.08). The sensing element, comprised of a platinum film on glass, had a diameter of 0.001 inch and was designed for temperature environments up to 1200° F. The sensor was oriented perpendicular to the mean flow direction and, consequently, provided a measure of velocity fluctuations parallel to the mean flow direction.

Calibration of the sensor was obtained by varying the mean velocity at constant temperature and plotting the sensor power as a function of the square root of mass flux density. Five points were generally used to establish the calibration, which was quite linear over the range of flows investigated.

PROCEDURE

All tests were conducted at a nominal stagnation pressure of 300 pounds per square inch absolute at a stagnation temperature of 970° R. Approximately $1\frac{1}{2}$ hours were required for the system to reach equilibrium. When equilibrium was approached, the bypass bleed flow rate was established in order to produce a uniform inlet velocity profile. The optimum bleed flow rate was determined by a combination of three methods; namely, (1) observation of the direct current output of the hot film sensor on an X-Y recorder, (2) observation of the pitot pressure on the X-Y recorder, and (3) measurement of the static pressure difference between the inner and outer surfaces of the airfoil-shaped cylindrical inlet lip.

The length of a typical steady-state run was about 2 hours, as dictated by the response time of the boundary layer pressure probes. All data, with the exception of the boundary layer pitot pressures, were obtained in a 15 minute interval. Each temperature was recorded 10 times on the automatic voltage digitizer in order to confirm the established steady-state conditions. Bourdon gages were read and the manometers were photographed four times in the same period. During the 2-hour span when boundary layer pressures were obtained, stagnation pressure drift was limited to about ±0.5 pound per square inch and the stagnation temperature varied by ±1.5° F; however, during the 15-minute data recording interval these tolerances were reduced to approximately ±0.25 pound per square inch and ±0.5° F, respectively.

EXPERIMENTAL RESULTS

Nozzle Pressure Distribution

Static-to-total pressure ratios for the conical nozzle are shown in figure 6 and table II. A characteristic deviation from one-dimensional values can be noted in the neighborhood of the throat.

Experimental pressure ratios are in good agreement with the data of refer-

TABLE II. - COMPARISON OF EXPERIMENTAL AND ONE-DIMENSIONAL PRESSURE RATIOS FOR 30°-15° CONICAL NOZZLE

Pressure tap	Ratio of axial distance to throat diameter, x/D_t	Area ratio, ϵ	Pressure ratio, P/P_0		
			One-dimensional	Experimental	Percent deviation
1	-3.026	17.436	0.9992	0.9999	0.07
2	-2.356	11.593	.9983	.9992	.09
3	-1.684	6.910	.9950	.9963	.13
4	-1.446	5.541	.9922	.9939	.17
5	-1.214	4.351	.9874	.9895	.21
6	-.979	3.299	.9779	.9812	.34
7	-.744	2.385	.9568	.9633	.67
8	-.411	1.382	.8546	.8413	-1.58
8a	-.241	1.116	.7385	.7101	-4.00
9	-.117	1.027	.6365	.5723	-11.2
10	.000	1.000	.5283	.4585	-15.2
11	.087	1.013	.4500	.3731	-20.6
12	.171	1.054	.3755	.2778	-35.1
13	.263	1.150	.2886	.2044	-41.1
14	.425	1.335	.2035	.1822	-11.7
15	.818	1.873	.1056	.1108	4.65
16	1.834	3.639	.0346	.0374	7.50
17	3.665	8.368	.0096	.0092	-4.35
18	5.497	15.008	.0040	.0038	-5.26
19	7.394	23.992	.0020	.0022	10.0

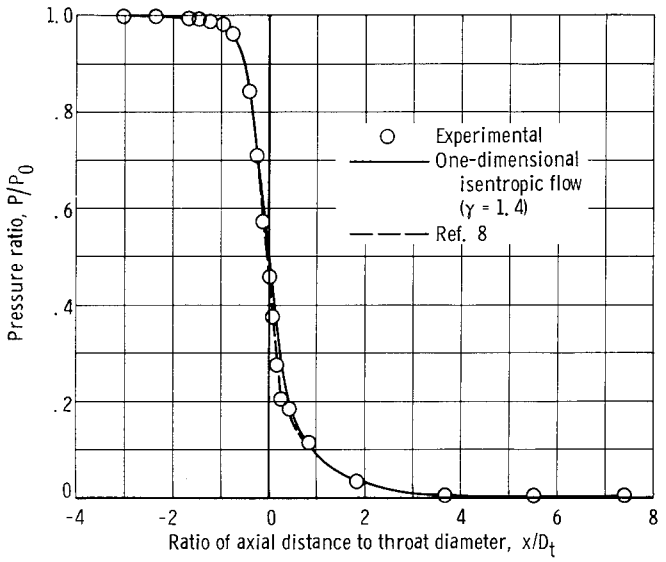

Figure 6. - Pressure ratio for conical nozzle in air. Total pressure, 300 pounds per square inch absolute; total temperature, 967° R; throat diameter, 1.492 inches.

ence 8 and others for conical nozzles of similar geometry (fig. 6). The maximum deviation of -41.1 percent from one-dimensional values occurred at an area ratio of 1.15 downstream of the throat.

Wall Temperature Distribution

The Fourier conduction equation for one-dimensional steady-state heat transmission was used in conjunction with the measurements obtained with the heat flux meter of figure 4 to determine gas-side nozzle-wall temperatures and local heat-transfer rates. The linear variation of thermal conductivity with temperature, determined by a calibration of the Inconel plug material, was incorporated in the equation. Integration of

TABLE III. - HEAT-FLUX METER AND NOZZLE WALL TEMPERATURES

[Total temperature, 958.1 °R; total pressure, 299.5 psia.]

Heat-flux meter	Ratio of axial distance to throat diameter, x/D_t	Heat-flux meter temperature, T, °F			Wall temperature, T_w, °F				Wall temperature, T_w, deviation from average, percent		
		Thermocouple			Thermocouple						
		a	b	c	a and b	a and c	b and c	average	a and b	a and c	b and c
1	-3.026	193.6	159.0	125.8	223.7	221.0	223.1	222.6	0.5	-0.7	0.2
2	-2.356	210.1	172.4	-----	246.0	-----	-----	-----	----	----	----
3	-1.684	245.5	197.5	155.7	289.3	277.9	286.6	284.6	1.7	-2.4	.7
4	-1.446	260.4	215.8	168.1	302.4	303.0	302.6	302.7	-.1	.1	.0
5	-1.214	273.3	224.7	175.9	319.5	320.8	319.8	320.0	-.2	.2	.0
6	-.979	279.0	227.7	172.3	336.1	340.4	337.2	337.9	-.5	.7	-.2
7	-.744	295.0	238.2	177.4	356.7	349.9	354.8	353.8	.8	-1.1	.3
8	-.411	319.4	259.0	198.6	374.3	370.0	373.2	372.5	.5	-.7	.2
9	-.117	319.9	257.6	196.0	372.1	368.7	371.3	370.7	.4	-.6	.2
10	.000	310.8	252.6	192.4	369.3	361.3	367.2	365.9	.9	-1.3	.4
11	.087	308.7	250.2	193.1	363.6	354.8	361.4	359.9	1.0	-1.4	.4
12	.171	302.7	265.1	194.0	338.1	383.6	349.9	357.2	-5.4	7.4	-2.0
13	.263	293.3	239.4	181.4	340.3	336.5	339.3	338.7	.5	-.7	.2
14	.425	280.6	232.0	177.4	327.2	329.3	327.8	328.1	-.3	.4	-.1
15	.818	258.5	217.9	166.9	302.6	301.5	302.3	302.1	.2	-.3	.1
16	1.834	207.9	170.2	132.2	238.7	236.8	238.2	237.9	.3	-.4	.1
17	3.665	122.5	103.1	86.1	140.3	135.4	139.1	138.3	1.5	-2.1	.6
18	5.497	84.7	73.1	60.8	95.3	96.3	95.5	95.7	-.5	.6	-.1
19	7.394	78.4	67.7	58.8	88.4	84.8	87.5	86.9	1.7	-2.4	.7

the conduction equation yields a temperature distribution of the following form:

$$-qy = \frac{mt}{2} + k_o t + \mathscr{C} \qquad (1)$$

The unknowns q and $\mathscr{C}$ were determined by the simultaneous solution of two equations by using the shaft temperature t and corresponding location y at any two stations along the heat-flux meter. Subsequently, the wall temperature was computed by setting y = 0.

Measurement of three temperatures along the meter shaft provided three possible combinations of variables for computing the nozzle wall temperature. If the arithmetic average of the three wall temperatures (in °F) agreed within ±2 percent of the values computed by each pair of temperatures, only the average value was used in subsequent calculations of heat-transfer coefficients. If any of the three wall temperatures exceed ±2 percent of the average value, the three temperatures plus the average value were used in the computation of heat-transfer coefficients. Shaft and wall temperatures are listed in table III for a typical run in which the total temperature was 958.1° R at a total pressure of 299.5 pounds per square inch absolute. The wall temperature in °F, as computed from each pair of thermocouples, was generally within about ±1.0 percent of the arithmetic average of the three wall temperatures.

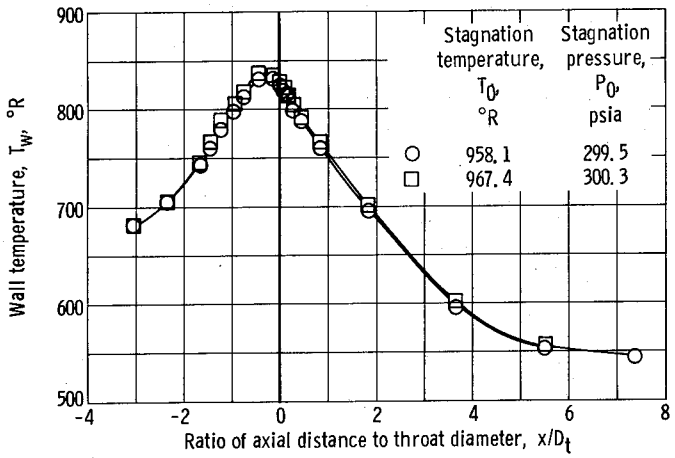

Figure 7. - Nozzle wall temperature distribution. Throat diameter, 1.492 inches.

TABLE IV. - CENTERLINE TURBULENCE LEVELS WITH AND WITHOUT THE UPSTREAM TURBULENCE GENERATOR.

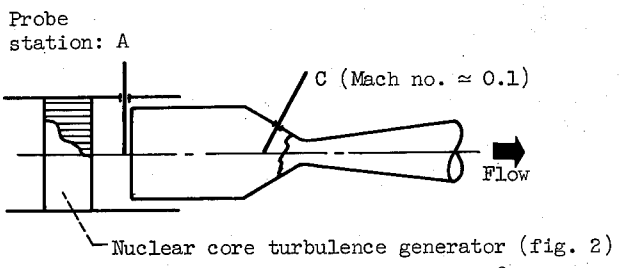

[Stagnation temperature, T_0, ≃ 968° R; stagnation pressure, P_0, 300 psia.]

	Bleed flow optimized			
	Turbulence		No turbulence	
	Station			
	A	C	A	C
$\frac{\rho\sqrt{\overline{u'^2}}}{\overline{\rho u}}$	0.101	0.018	0.028	-----
$\overline{\rho u}$, lb/(ft^2)(sec)	39.3	121.0	39.0	-----
$\rho\sqrt{\overline{u'^2}}$, lb/(ft^2)(sec)	4.0	2.2	1.1	-----

The wall temperature distribution for the nozzle is shown in figure 7. Data are presented for two runs in which the stagnation temperatures differed by 9.3° R. The sensitivity of the heat-flux meters to this modest difference in stagnation temperature is reflected in a slight shift in the wall temperature distribution curve. The ratio of peak wall temperature (839.4° R) to a stagnation temperature of 967.4° R was similar to that of reference 5 ($T_w/T_0 \simeq 0.85$) for a nozzle of similar upstream geometry but operating at a stagnation temperature of 1600° R.

Turbulence Measurements

The ratio of turbulence intensity to the local time average value $\rho\sqrt{\overline{(u')^2}}/\overline{\rho u}$ at the centerline 1/4 inch upstream of the plane of the cylindrical inlet leading edge varied from 0.101 with the turbulence generator to 0.028 with no upstream turbulence generator (table IV). These values were obtained for a bleed flow rate that provided the most uniform inlet velocity profile. Further reference to data in which the turbulence generator was used will be confined to this optimized bleed flow rate.

Turbulence intensity profiles in a plane 1/4 inch upstream of the cylindrical inlet are presented in figure 8. In the absence of the upstream turbulence generator, the turbulence intensity profile was essentially uniform; for example, $\rho\sqrt{\overline{(u')^2}}/\overline{\rho u}$ ranged from about 0.028 at the centerline to 0.035 near the wall of the cylindrical inlet. With the turbulence gener-

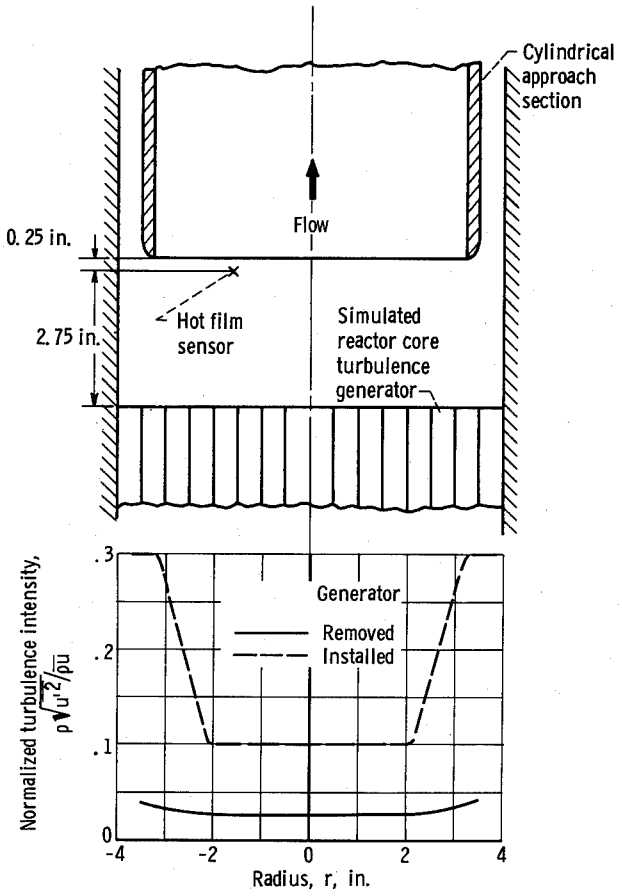

Figure 8. - Turbulence intensity profiles at cylindrical inlet for optimized bleed flow rates.

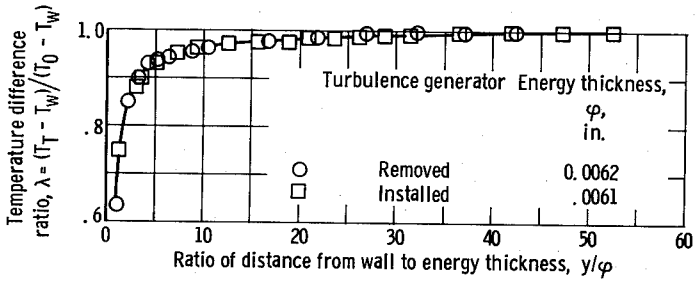

Figure 9. - Temperature profiles at convergent nozzle probing station with and without turbulence generator.

ator installed, however, turbulence levels approaching a value of 0.3 were obtained near the inlet leading edge.

It can also be noted in figure 8 that the diameter of the core of uniform turbulence level was appreciably less than the inlet diameter. The inability to achieve the desired uniform core across the cylindrical inlet was attributed to blockage in the bleed flow annulus resulting from the turbulence generator support.

A hot film sensor was also installed at station C in the nozzle to ascertain the extent of centerline turbulence decay for upstream turbulence generation (table IV). A comparison of measurements at stations A and C indicates that the turbulence intensity ratio $\rho\sqrt{\overline{(u')^2}}/\overline{\rho u}$ diminishes greatly as the flow passes through the cylindrical inlet and nozzle entrance. Values of $\rho\sqrt{\overline{(u')^2}}/\overline{\rho u}$ decayed from 10.1 to 1.8 percent. The level of the fluctuating components $\rho\sqrt{\overline{(u')^2}}$ decreased by about a factor of two between stations A and C (table IV).

Boundary Layer Profiles

Stagnation temperature distribution. - The boundary layer stagnation temperature distribution for the convergent section of the nozzle (Mach number, 0.08) is presented in figure 9 in terms of the difference ratio λ as a function of the dimensionless distance y/φ. The temperature difference ratio λ and the energy thickness φ, are

given by the following equations:

$$\lambda = \frac{T_T - T_w}{T_{T,e} - T_w} \tag{2}$$

$$\varphi = \int_0^\infty \frac{\rho u}{\rho_e u_e} \left[1 - \left(\frac{T_T - T_w}{T_{T,e} - T_w} \right) \right] dy \tag{3}$$

In the above expressions, it was assumed that $T_{T,e} \simeq T_0$ because the Mach number was low (0.08) and that the radius R of the measuring station is much larger than φ.

The temperature distributions for the convergent nozzle probing station in figure 9 are presented for runs with and without the upstream turbulence generator for a nominal total temperature and pressure of 968° R and 300 pounds per square inch absolute, respectively. The energy thickness (approx 0.006 in.) and temperature profiles were nearly identical for the two cases indicating that the upstream turbulence generator had little effect on the boundary layer temperature distribution.

In the uncooled cylindrical inlet, the departure from a uniform stagnation temperature distribution was essentially negligible ($\lambda \simeq 0$) for all runs, with and without upstream turbulence and, therefore, will not be presented.

Velocity profiles. - The velocity head $P_T - P_s$ measured in the boundary

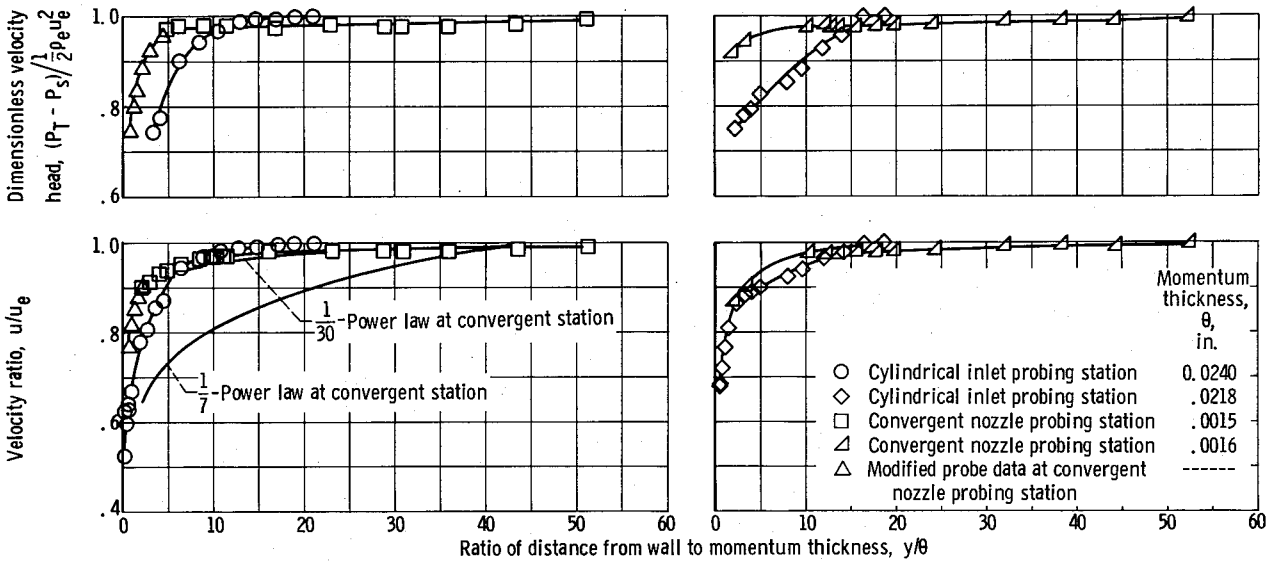

(a) Without turbulence generator. Stagnation temperature, 967.4° R; stagnation pressure, 300.3 pounds per square inch absolute.

(b) With turbulence generator. Stagnation temperature, 969.7° R; stagnation pressure, 296.45 pounds per square inch absolute.

Figure 10. - Velocity profiles at cylindrical inlet and convergent nozzle probing stations.

layer was converted to velocity by locally applying the incompressible Bernoulli equation. In the cylindrical inlet the density through the boundary layer was assumed constant since the wall was uncooled; however, in the convergent part of the nozzle where heat transfer was present, it was necessary to account for the boundary layer density gradient. In figures 10(a) and (b), the dimensionless velocity head $(P_T - P_s)/\frac{1}{2}\rho_e u_e^2$ and velocity u/u_e are presented as functions of the distance from the wall y nondimensionalized by the momentum thickness θ, where θ is given by the following equation:

$$\theta = \int_0^\infty \frac{\rho u}{\rho_e u_e}\left(1 - \frac{u}{u_e}\right) dy \tag{4}$$

The velocity profiles in figure 10(a) are for the case of no upstream turbulence generation, and those of figure 10(b) include the effects introduced by the simulated reactor core turbulence generator.

In figure 10(a), the nondimensional velocity head curve for the nozzle convergence section includes data obtained with a modified probe and recording system. The modified system, which permitted measurements closer to the wall, was used to generate the shape of the velocity head curve in the region near the wall.

A velocity profile corresponding to the commonly assumed 1/7-power law is shown for the convergent station in figure 10(a). Obviously, the experimental velocity profile was significantly different (more nearly approximated by a 1/30-power law).

The turbulence generator produced only a slight change in the nozzle convergence station velocity profile; however, a pronounced difference in profile shape can be noted in the cylindrical inlet station. This latter difference in shape is attributed to the nonuniform inlet velocity profile produced by the turbulence generator (discussed previously in the section Turbulence Measurements).

In determining the experimental momentum thickness at the convergent measuring station, the velocity profile was extrapolated to zero in three different ways. These extrapolations (due to lack of measurements at $y < 0.001$ in.) contributed an error of approximately 20 percent in the momentum thickness. Although this error is significant, a greater error in the momentum thickness results from the almost flat velocity profile, which makes it extremely difficult to determine the boundary layer termination point. The importance of this boundary layer termination is further increased by the fact that the contribution at this outer region of the boundary layer to the momentum thickness is very significant. The integrand of the momentum thickness through the boundary layer gives a graphical visualization of this contribution (outer boundary layer region) to the momentum thickness (fig. 11). In order to show the greatly changed character of the boundary layer in the convergent region compared with the cylindrical inlet section, the integrand of the momentum thickness at the

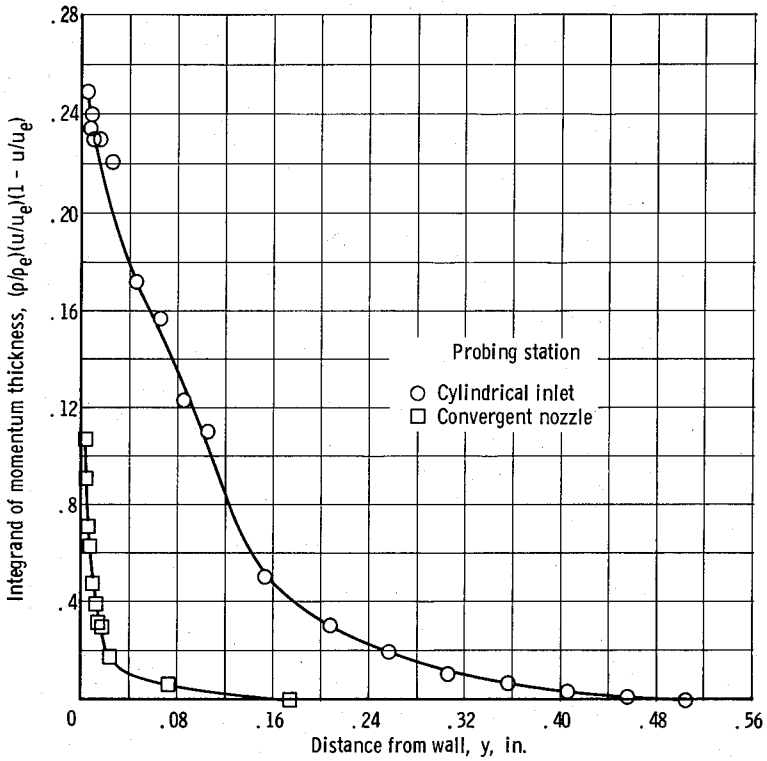

Figure 11. - Variation of integrand of momentum thickness across boundary layer for cylindrical inlet and convergent nozzle probing stations.

probing station in the cylindrical inlet section is also plotted in figure 11. With these difficulties considered (lack of data near the wall and inaccurate boundary layer termination), approximately 80 to 120 percent error in the momentum thickness can be expected for the convergent nozzle probing station.

Experimental values of momentum thickness are listed in figure 10. Momentum thicknesses for the cylindrical inlet were nearly an order of magnitude greater than the values for the convergence probing station. Cold flow tests produced no significant change in the momentum, displacement, or boundary layer thickness at the convergent section probing station compared with the hot flow tests. Therefore, the greatly reduced boundary layer thickness and drastically changed velocity profile in the convergent section compared with the cylindrical inlet section can be attributed primarily to acceleration effects. Addition of the turbulence generator produced little change in momentum thickness at both stations.

In figure 12, the shear velocity profile for the cylindrical inlet station is shown in terms of u^+ and y^+, which are given in reference 9 as follows:

$$u^+ = \frac{u}{u_e}\sqrt{\frac{2\rho_w}{C_f\rho_e}} \tag{5}$$

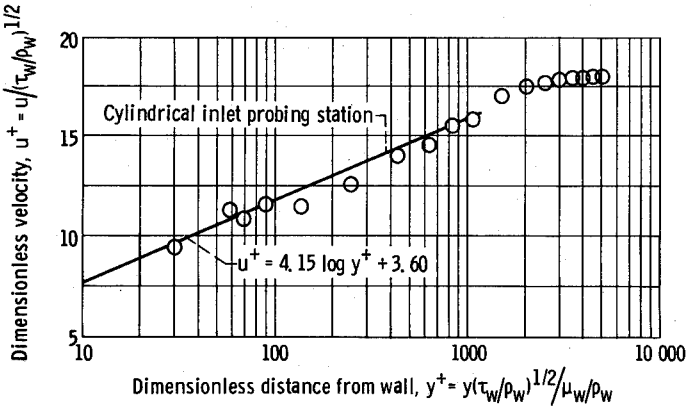

Figure 12. - Shear velocity distribution at cylindrical inlet probing station. Stagnation temperature, 967.4° R; stagnation pressure, 300.3 pounds per square inch.

$$y^+ = \frac{\rho_w u_e y}{\mu_w} \sqrt{\frac{C_f \rho_e}{2\rho_w}} \tag{6}$$

The skin friction coefficient C_f was determined from the experimental data in conjunction with the von Kármán equation for the "law of the wall" (ref. 10), which can be written in the following form:

$$u^+ = \frac{u}{u_e} \sqrt{\frac{2}{C_f}}$$

$$= 4.15 \log\left(\frac{y}{\theta} \mathrm{Re}_\theta \sqrt{\frac{C_f}{2}}\right) + 3.60 \tag{7}$$

The experimental data in figure 12 are in good agreement with the von Kármán form of the law of the wall up to a value of $y^+ \simeq 1000$ thus confirming the presence of a turbulent boundary layer in the cylindrical approach section. In the outer part of the boundary layer ($y^+ > 1000$) a departure from the law of the wall can be noted. This departure, referred to as the "law of the wake" (ref. 11), is characteristic of turbulent boundary layers.

The data of figure 12 tacitly indicate that boundary layer measurements could not be obtained in the thin sublayer that terminates at $y^+ \simeq 26$.

Heat-transfer coefficient. - Experimental values of the heat-transfer coefficient based on enthalpy were determined from the following equation:

$$h_i = \frac{q}{i_{ad} - i_w} \tag{8}$$

where the adiabatic enthalpy i_{ad} was given by

$$i_{ad} = i_s + \mathrm{Pr}^{1/3} (i_0 - i_s) \tag{9}$$

The Prandtl number was assumed constant at 0.7. The static and total enthalpies i_s and i_0, respectively, were computed by an iteration procedure by using the equations of reference 12 for entropy, enthalpy, and specific heat.

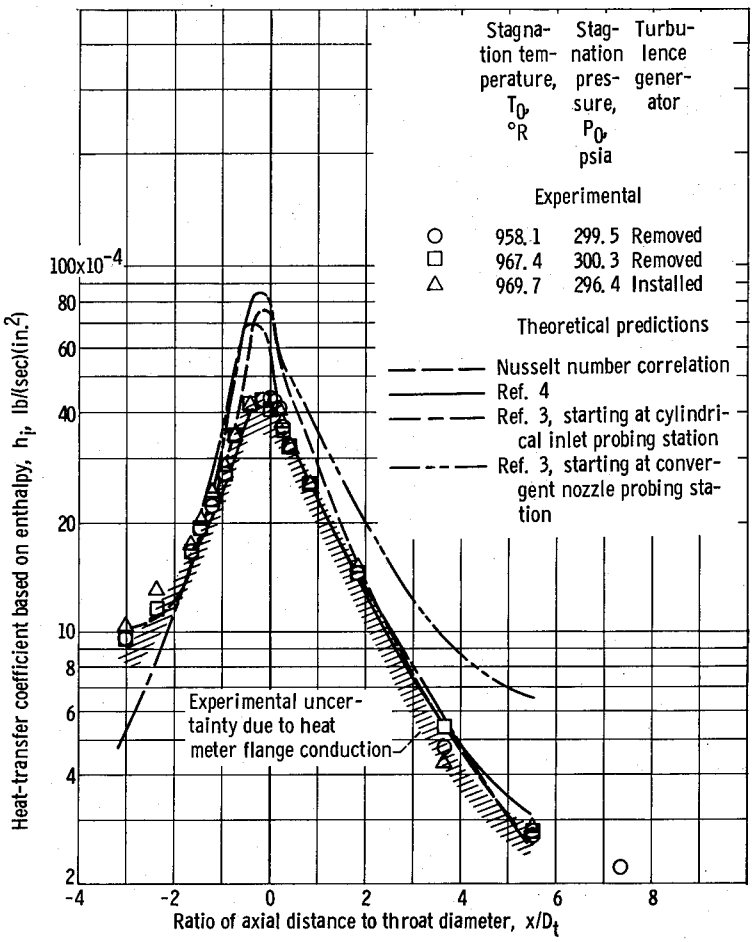

Figure 13. - Variation of experimental heat-transfer coefficient along nozzle and comparison with theoretical predictions. Throat diameter, 1.492 inches.

Experimental values of the heat-transfer coefficient are presented in figure 13 and table V for runs with and without the reactor core turbulence generator. Also shown are heat-transfer distributions resulting from various theoretical prediction techniques; however, discussion of these curves will be deferred until the following section. The experimental heat-transfer distributions of figure 13 were duplicated to within about ±2 percent in several runs; however, for reasons of clarity, only the data for two runs without upstream turbulence generation and one run with the simulated reactor core turbulence generator are presented.

The turbulence generator, installed 3 inches upstream of the cylindrical inlet, produced an inlet turbulence level $\rho\sqrt{\overline{(u')^2}}/\overline{\rho u}$ of 10.1 percent, as compared with a 2.8-percent value without the generator. Although a decay in these normalized values of turbulence was encountered as the flow passed through the inlet and nozzle entrance regions, the absolute turbulence intensity $\rho\sqrt{\overline{(u')^2}}$ at station C was about a factor of two higher than the upstream value with no generator. As noted in figure 13, heat-transfer coefficients were essentially unaltered even with the higher levels of turbulence intensity (table IV).

The maximum heat-transfer coefficient, occurring slightly upstream of the geometric throat, was about 0.0044 pound per second per square inch with and without the upstream turbulence generator. It is interesting to note that the maximum heat-transfer coefficient in this investigation was approximately 80 percent of the value obtained in reference 5 for a nozzle with the same convergence and throat geometry. Both nozzles operated at the same nominal total pressure (300 lb/sq in. abs), but the nozzle of reference 4 was tested at a total temperature of 1600° R rather than 960° R. The higher temperature resulted in lower values of mass flux ρu. Therefore, from a strict mass flux consideration in which $h \propto (\rho u)^{0.8}$, the values of heat-transfer coefficient in this investigation would be expected to slightly exceed those of reference 5. It is expected, however, that the differences in the heat-transfer coefficient may arise because of the influence of upstream geometry and acceleration on the boundary layer growth at the nozzle entrance.

COMPARISON WITH THEORETICAL METHODS

The experimental data are compared with results from the three following calculation methods:

(1) Nusselt number correlation

(2) Compressible boundary layer theory (ref. 3)

(3) Incompressible boundary layer theory (ref. 4)

Values of the heat-transfer coefficients obtained by the above methods are given in table V.

The heat-transfer coefficient calculated from the Nusselt number correlation and evaluated at the reference enthalpy is given by

$$h = \frac{k_{ref} Nu_{ref}}{12\ C_{p,ref} D} \tag{10}$$

The subscript ref indicates the the flow properties are evaluated at the reference enthalpy condition and the Nusselt number Nu_{ref}:

$$Nu_{ref} = 0.026\ Re_{D,ref}^{0.8} Pr^{1/3} \tag{11}$$

where the Prandtl number Pr is assumed constant at 0.71 and the Reynolds number $Re_{D,ref}$ based on the diameter of the nozzle at each station and evaluated at the reference enthalpy is given by

$$Re_{D,ref} = \frac{\rho_{ref} u_e D}{\mu_{ref}} \tag{12}$$

TABLE V. - EXPERIMENTAL AND PREDICTED NOZZLE HEAT-TRANSFER COEFFICIENTS

[Total temperature, $\simeq 960.0^{\circ}$ R; total pressure, 300.0 psia.]

Ratio of axial distance to throat diameter, x/D_t	Heat-transfer coefficient based on enthalpy, h_i, lb/(sec)(in.^{2})					
	Experiment with turbulence generator	Experiment without turbulence generator	Nusselt number correlation	Boundary layer theory (ref. 3)		Arbitrary wall temperature method (ref. 4)
				Cylindrical inlet starting point	Nozzle starting point	
-3.026	10.40×10^{-4}	9.63×10^{-4}	10.48×10^{-4}	4.83×10^{-4}	----------	----------
-2.356	13.19	----------	10.94	9.42	----------	----------
-1.684	17.69	16.81×10^{-4}	15.49	15.63	----------	15.90×10^{-4}
-1.446	20.37	19.46	18.23	18.25	21.17×10^{-4}	18.01
-1.214	24.02	22.35	22.26	23.92	27.21	21.07
-.979	28.21×10^{-4}	27.32×10^{-4}	27.85×10^{-4}	33.84×10^{-4}	36.79×10^{-4}	25.50×10^{-4}
-.744	34.93	34.87	36.49	55.84	51.67	39.11
-.411	42.42	42.95	65.28	68.76	77.92	38.22
-.117	----------	43.84	75.75	64.59	85.01	43.36
.000	----------	43.61	72.78	54.17	75.84	42.95
.087	----------	42.17×10^{-4}	67.74×10^{-4}	47.09×10^{-4}	68.34×10^{-4}	41.59×10^{-4}
.171	39.74×10^{-4}	41.03	59.01	42.92	56.25	34.83
.263	36.48	36.63	49.65	38.96	55.42	34.40
.425	32.53	32.59	46.25	35.25	52.09	33.74
.818	25.65	25.43	33.48	29.79	40.09	26.75
1.834	15.11×10^{-4}	14.74×10^{-4}	15.58×10^{-4}	14.83×10^{-4}	21.04×10^{-4}	14.65×10^{-4}
3.665	4.34	4.80	5.44	5.75	9.33	5.44
5.497	2.88	2.77	2.68	2.69	6.46	3.15
7.394	----------	2.23	1.75	----------	----------	----------

In figure 13 the Nusselt number correlation based on reference enthalpy gives approximately a 70-percent greater heat-transfer coefficient at the nozzle throat than that given by the experimental data. Similarly, the compressible boundary layer calculation (ref. 3) predicts a 60-percent higher heat-transfer coefficient near the throat than that of the experimental data. This calculation starts at the probing station in the cylindrical inlet by using the boundary layer thicknesses measured there. Also, a similar calculation, which starts at the convergent nozzle probing station and uses the measured boundary layer thicknesses, predicts a 93-percent higher heat-transfer coefficient near the throat than that of the experimental data.

This theoretical boundary layer calculation (ref. 3) is based on flat plate (zero acceleration) heat-transfer theory. Therefore, not only the 1/7-power velocity profile but also the skin friction coefficient and Reynolds analogy are based on the flat plate theory. Comparison of this compressible boundary layer theory with the experimental data at the convergent probing station gives the following results:

(a) The experimental velocity profile was not represented by the usually assumed 1/7-power law (fig. 10(a)).

(b) The experimental momentum thickness is a factor of 4 less than the calculated value for a free stream Mach number of 0.08 based on reference 3.

(c) The experimental displacement thickness is about a factor of 10 less than the calculated value based on reference 3.

This comparison indicates that the 1/7-power profile does not describe a nozzle boundary layer distribution; however, the sensitivity of the integral calculation of heat transfer to the profile shape is questionable. In reference 13, boundary layer shape parameters were relatively insensitive to profile powers of 1/5 to 1/11; however profiles approaching a 1/30 power law, as experienced in the present study, may have an appreciable influence on the heat transfer. Also, significant errors in the flat-plate Reynolds analogy as applied to nozzle flows will greatly change the heat transfer. This is primarily caused by the direct sensitivity of the Reynolds analogy and skin friction coefficient in the integral calculation of the heat transfer.

The incompressible boundary layer theory of reference 4, which is based on incompressible flat plate theory but includes variations in wall temperature, predicted the heat-transfer coefficient very well. Heat-transfer coefficients at the throat were within about 2 percent of the experimental results; however, this excellent correlation with experimental data may be a result of compensating errors in the flat plate theory as applied to the present nozzle geometry and flow conditions. Compensating errors are expected especially since the predicted ratio of the thermal to velocity boundary layer thickness at the convergent nozzle probing station is approximately 150 percent greater than the measured value. Therefore caution is suggested when applying this heat-transfer calculation method to nozzle flow.

SUMMARY OF RESULTS

Experimental velocity and temperature profiles in the boundary layer, heat-transfer, and turbulence measurements have been presented for a conical nozzle configuration with a cylindrical approach section operating in air at a nominal total temperature and pressure of 960° R and 300 pounds per square inch absolute, respectively. An analysis of the results of this investigation has indicated the following:

1. Experimental heat-transfer coefficients could not be correlated by either of the following methods: (1) a Nusselt-type pipe flow correlation and (2) a compressible integral boundary layer prediction technique. Predicted values of the heat-transfer coefficient were significantly higher than the experimental values in the convergent and throat region of the nozzle.

Application of an incompressible boundary layer technique resulted in good agreement between predicted and experimental nozzle heat-transfer coefficients. Predicted values in the throat region were within about 2 percent of the experimental results; however, the agreement may be fortuitous since the predicted ratio of the thermal to boundary layer thickness at the convergent nozzle probing station was approximately 150 percent greater than the measured value. Therefore caution should be observed with regard to a generalization of these results.

2. The introduction of a simulated reactor core turbulence generator upstream of the cylindrical inlet resulted in very high levels of inlet turbulence (ratio of root-mean-square velocity to time-averaged value ≥ 0.10) as well as a nonuniform turbulence profile; however, these normalized turbulence levels were much lower in the nozzle convergence section ($\simeq 0.02$). Consideration of only the fluctuating component of turbulence intensity in the convergent part of the nozzle reveals that the value was about two times the upstream value with no turbulence generator. The effect on nozzle heat-transfer coefficients resulting from this disturbed flow was negligible.

3. The experimental momentum thickness was a factor of 4 less than the value calculated by a compressible boundary layer prediction technique. The corresponding displacement thickness was a factor of 10 less than the predicted value.

4. The greatly reduced boundary layer thicknesses and much steeper velocity profiles in the convergent section compared with those of the cylindrical inlet section can be attributed primarily to acceleration effects.

Lewis Research Center,
National Aeronautics and Space Administration,
Cleveland, Ohio, October 11, 1965.

REFERENCES

1. Bartz, D. R.: A Simple Equation for Rapid Estimation of Rocket Nozzle Convective Heat Transfer Coefficients. Jet Prop., vol. 21, no. 1, Jan. 1957, pp. 49-51.

2. Bartz, D. R.: An Approximate Solution of Compressible Turbulent Boundary-Layer Development and Convective Heat Transfer in Convergent-Divergent Nozzles. Trans. ASME, vol. 77, no. 8, Nov. 1955, pp. 1235-1245.

3. Elliott, David G.; Bartz, Donald R.; and Silver, Sidney.: Calculation of Turbulent Boundary-Layer Growth and Heat Transfer in Axi-Symmetric Nozzles. Rept. No. 32-387, Jet Prop. Lab., C.I.T., Feb. 1963.

4. Reynolds, W. C.; Kays, W. M.; and Kline, S. J.: Heat Transfer in the Turbulent Incompressible Boundary Layer. III - Arbitrary Wall Temperature and Heat Flux. NASA MEMO 12-3-58W, 1958.

5. Fortini, Anthony; and Ehlers, Robert C.: Comparison of Experimental to Predicted Heat Transfer in a Bell-Shaped Nozzle with Upstream Flow Disturbances. NASA TN D-1743, 1963.

6. Neumann, Harvey E.; and Bettinger, Paula J.: A Comparative Analysis of Convective Heat Transfer in a Nuclear Rocket Nozzle. NASA TN D-1742, 1963.

7. Schacht, Ralph L.; Quentmeyer, Richard J.; and Jones, William L.: Experimental Investigation of Hot-Gas Side Heat-Transfer Rates for a Hydrogen-Oxygen Rocket. NASA TN D-2832, 1965.

8. Back, L. H.; Massier, P. F.; and Gier, H. L.: Comparisons of Experimental With Predicted Wall Static-Pressure Distributions in Conical Supersonic Nozzles. Tech. Rept. No. 32-654, Jet Propulsion Lab., Calif. Inst. of Tech. (NASA CR-59577), Oct. 1964.

9. Deissler, R. G.; and Loeffler, A. L., Jr.: Analysis of Turbulent Flow and Heat Transfer on a Flat Plate at High Mach Numbers with Variable Fluid Properties. NASA TR R-17, 1959.

10. von Kármán, Th.: Turbulence and Skin Friction. J. Aero. Sci., vol. 1, no. 1, Jan. 1934, pp. 1-20.

11. Coles, Donald: The Law of the Wake in the Turbulent Boundary Layer. J. Fluid Mech., vol. 1, pt. 1, May 1956, pp. 191-226.

12. McBride, Bonnie J.; Heimel, Sheldon; Ehlers, Janet G.; and Gordon, Sanford: Thermodynamic Properties to 6000° K for 210 Substances Involving the First 18 Elements. NASA SP-3001, 1963.

13. Tucker, Maurice: Approximate Calculation of Turbulent Boundary-Layer Development in Compressible Flow. NACA TN 2337, 1951.

NASA-Langley, 1966 E-3065

"The aeronautical and space activities of the United States shall be conducted so as to contribute . . . to the expansion of human knowledge of phenomena in the atmosphere and space. The Administration shall provide for the widest practicable and appropriate dissemination of information concerning its activities and the results thereof."

—NATIONAL AERONAUTICS AND SPACE ACT OF 1958

NASA SCIENTIFIC AND TECHNICAL PUBLICATIONS

TECHNICAL REPORTS: Scientific and technical information considered important, complete, and a lasting contribution to existing knowledge.

TECHNICAL NOTES: Information less broad in scope but nevertheless of importance as a contribution to existing knowledge.

TECHNICAL MEMORANDUMS: Information receiving limited distribution because of preliminary data, security classification, or other reasons.

CONTRACTOR REPORTS: Technical information generated in connection with a NASA contract or grant and released under NASA auspices.

TECHNICAL TRANSLATIONS: Information published in a foreign language considered to merit NASA distribution in English.

TECHNICAL REPRINTS: Information derived from NASA activities and initially published in the form of journal articles.

SPECIAL PUBLICATIONS: Information derived from or of value to NASA activities but not necessarily reporting the results of individual NASA-programmed scientific efforts. Publications include conference proceedings, monographs, data compilations, handbooks, sourcebooks, and special bibliographies.

Details on the availability of these publications may be obtained from:

SCIENTIFIC AND TECHNICAL INFORMATION DIVISION

NATIONAL AERONAUTICS AND SPACE ADMINISTRATION

Washington, D.C. 20546